

Research Report

Subject: Lensless in-line holographic microscopy

Student: Songhui Wang

Tutor: Prof. Yaneck Gottesman

September 1, 2025

Abstract

Lensless in-line holographic microscopy (LIHM) is a compact and cost-effective imaging technique that records diffraction patterns directly on a sensor and reconstructs both amplitude and phase numerically. In this work, I develop a Python-based simulation framework that models hologram formation using the angular spectrum method and implements iterative phase retrieval with additional constraints. The simulation incorporates practical factors such as noise, partial coherence, sampling, and pixel-integration effects providing realistic predictions of reconstruction quality. I further analyze the resolution dependence on sample–sensor distance, illumination coherence, and sensor pixel pitch, establishing theoretical bounds and discussing on criteria for suitable samples.

Based on this framework, I construct a simple LIHM prototype using a narrowband LED source and a CMOS sensor and I validate reconstruction performance through experiments with a USAF resolution target. Additional tests with multi-exposure HDR holograms demonstrate that while faint fringes can be enhanced, reconstruction quality remains similar to single-exposure recordings under non-saturating conditions.

1 Introduction

Lensless in-line holographic microscopy (LIHM) records a sample’s diffraction pattern directly on an image sensor, without any lenses. The complex optical field is numerically reconstructed—using angular-spectrum forward/backward propagation and iterative phase retrieval—to form amplitude and phase images. By eliminating bulky objectives and lenses, LIHM is compact and offers a field of view defined by the sensor’s active region, low cost, and straightforward integration with portable devices. These attributes make LIHM attractive for medical diagnostics, field-deployable imaging, and resource-limited settings [1].

However, LIHM also faces well-known challenges. The in-line geometry introduces twin-image ambiguity and coherence-related artifacts. The reconstruction quality is sensitive to illumination bandwidth, sensor pixel pitch, wavelength, and sample–sensor distance. Achieving high resolution often requires multiple measurements—such as multi-angle illumination [2] or multi-height acquisition [3]—to satisfy sampling constraints via pixel super-resolution. Consequently, careful optical design, calibration, and computational modeling are therefore essential to realize robust, high-fidelity reconstructions.

This report presents my study of LIHM through simulation, system construction and experiments. (i) I develop a Python-based framework that models hologram formation and implements an iterative phase-retrieval reconstruction. (ii) I analyze how wavelength, sample–sensor distance and sensor pixel pitch affect image reconstruction. (iii) I build a compact LIHM prototype using only a narrowband LED array and a sensor with a pixel pitch of $5.86\ \mu\text{m}$. (iv) I validate the real reconstruction performance against the simulation framework.

Overall, this study connects computational modeling with a practical lensless microscope, offering suggestions for building and tuning LIHM systems.

2 LIHM simulation framework

Because our system employs a narrowband LED for illumination (the usage of an LED is preferred), I model the field at the sample as a quasi-monochromatic plane wave when the source is sufficiently far from the sample. When the wave goes through the sample, two beams are generated. One is called the reference beam as it is not affected by the sample and another is called the object beam because it is scattered by the sample. Then both fields propagate a distance from the sample plane to the sensor plane via angular spectrum method and their superposition forms the recorded hologram (intensity).

2.1 Theoretical background

My simulation starts from this hologram acquisition and perform the reconstruction based on the iterative phase retrieval algorithm. To have a better idea on this whole process, I summarize these helpful theoretical information.

2.1.1 Hologram and holography

In 1948, Dennis Gabor proposed a two-step, lensless imaging method that he called wavefront reconstruction, which is now known as holography. The key idea is to record the interference between a known reference beam and the object beam that has been diffracted or scattered by the sample. Although an image sensor measures only intensity, the interference encodes the relative phase into intensity variations, enabling phase retrieval in a subsequent reconstruction step.

For in-line holography, the unscattered component of the illumination serves as the reference wave R , while the scattered component forms the object wave O . The recorded intensity hologram is

$$I = |R + O|^2 = |R|^2 + |O|^2 + R^*O + RO^*. \quad (1)$$

$|R|^2$ is the background (typically uniform) which does not contain useful information regarding the objects. $|O|^2$ is the object's self-interference term and normally its intensity is very low compared with other terms so it can be neglected. In reconstruction, the hologram I is illuminated by the reference beam R so the last two terms in (1) give:

$$|R^2|O + R^2O^*. \quad (2)$$

the first term in (2) provides the object wave distribution. The second term shows the characteristic limitation of in-line holography which is the so-called twin-image. This term is the conjugation of the object wave and has a reverse curvature compared to the object wave [4].

2.1.2 Angular spectrum method

The angular spectrum method models scalar wave propagation between two parallel planes. It proceeds by (i) Fourier-transforming the field on the source plane, (ii) multiplying by the free-space transfer function, and (iii) inverse Fourier-transforming to obtain the field on the destination plane.

Let the complex field at $z = 0$ be $U(x, y, 0)$. Its angular spectrum is

$$A(f_x, f_y; 0) = \iint_{-\infty}^{\infty} U(x, y, 0) e^{-j2\pi(f_x x + f_y y)} dx dy. \quad (3)$$

The inverse relation is

$$U(x, y, 0) = \iint_{-\infty}^{\infty} A(f_x, f_y; 0) e^{j2\pi(f_x x + f_y y)} df_x df_y. \quad (4)$$

After propagating a distance z in free space, the spectrum must satisfy the Helmholtz equation $\nabla^2 U + k^2 U = 0$ with $k = 2\pi/\lambda$. Each plane wave component accumulates a phase given by

$$A(f_x, f_y; z) = A(f_x, f_y; 0) H(f_x, f_y; z), \quad H(f_x, f_y; z) = \exp\left\{j2\pi z \sqrt{\frac{1}{\lambda^2} - f_x^2 - f_y^2}\right\}. \quad (5)$$

Thus the propagated field is

$$U(x, y, z) = \iint_{-\infty}^{\infty} A(f_x, f_y; 0) H(f_x, f_y; z) e^{j2\pi(f_x x + f_y y)} df_x df_y. \quad (6)$$

Cutoff frequency. However, the transfer function deserves more attention. When

$$f_x^2 + f_y^2 < \frac{1}{\lambda^2}, \quad (7)$$

the square root in (5) is real and the effect of propagation is a pure phase delay (no change of amplitude). When $f_x^2 + f_y^2 > 1/\lambda^2$, the square root becomes purely imaginary and the transfer function can be written in this form

$$H(f_x, f_y; z) = \exp \left\{ -2\pi z \sqrt{f_x^2 + f_y^2 - \frac{1}{\lambda^2}} \right\}, \quad (8)$$

these wave components are exponentially attenuated during propagation and they are called evanescent waves. For typical propagation distances these components contribute negligibly, which imposes the well-known cutoff $f_x^2 + f_y^2 \leq 1/\lambda^2$ on the propagating spectrum[5].

Practical notes. With sampled data of spacing $\Delta x, \Delta y$ and array size $N_x \times N_y$, the discrete frequency grids are $f_x = \frac{u}{N_x \Delta x}$, $f_y = \frac{v}{N_y \Delta y}$ with u, v the integer frequency indices after `fftshift`.

2.1.3 Sampling and pixel–pitch constraints

By the Nyquist–Shannon sampling theorem, a band-limited signal of sampling frequency f_s can be perfectly recovered if the highest spatial frequency contained in the signal does not exceed the Nyquist frequency

$$f_N = \frac{f_s}{2}. \quad (9)$$

For a sensor with pixel pitch Δ (sampling step in x or y), the sampling frequency is $f_s = 1/\Delta$, hence

$$f_N = \frac{1}{2\Delta}. \quad (10)$$

In 2D, the sampled hologram must satisfy

$$|f_x| \leq \frac{1}{2\Delta_x}, \quad |f_y| \leq \frac{1}{2\Delta_y}, \quad (11)$$

otherwise spatial aliasing occurs and fine fringes fold back to lower frequencies, corrupting the reconstruction because this iterative phase retrieval algorithm cannot reliably recover aliased details. For example, Figure (1) below shows that aliasing can hugely degrade the reconstruction quality.

2.1.4 Source coherence

Usable in-line holograms require temporal and spatial coherence that are sufficient but not excessive to retain the interference term while avoiding coherence-induced artifacts. In practice, a narrowband, partially coherent source provides a good compromise.

Temporal coherence. The temporal coherence is mainly determined by the spectral bandwidth $\Delta\lambda$ of the system’s illumination. This temporal coherence implies the coherence length L_{coh} :

$$L_{coh} \approx \left(\frac{2 \ln 2}{\pi} \right) \frac{\lambda^2}{n \Delta\lambda}, \quad (12)$$

where n is the refractive index of the medium. The coherence length L_{coh} should exceed the optical path difference between the reference wave R and object wave O . Otherwise, some interference term is washed out. Conversely, if the temporal coherence is too strong, parasitic reflections (e.g., from the sensor cover glass) still remain coherent with R and generate unwanted fringes and speckle noise.

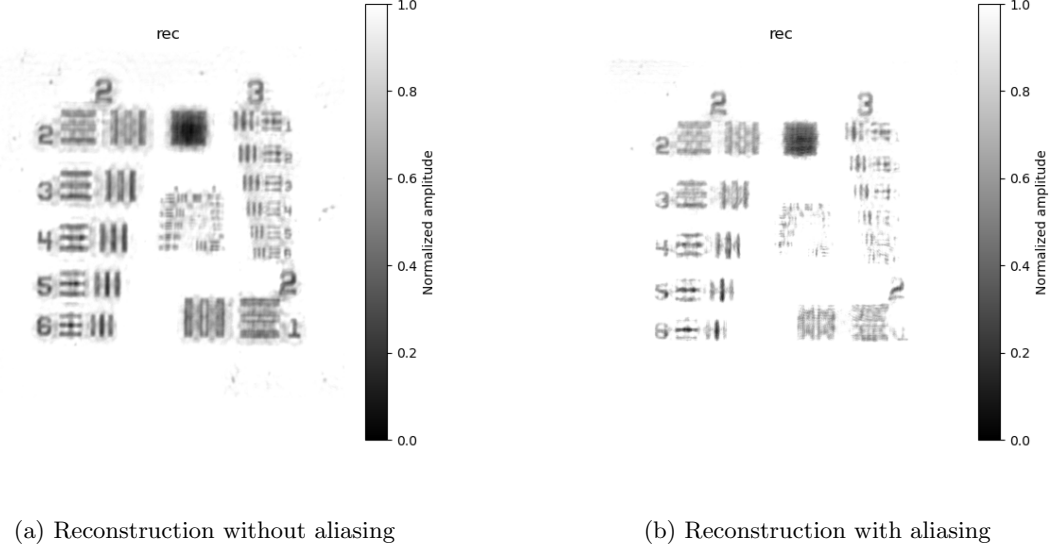


Figure 1: Reconstruction comparison

Spatial coherence. By the van Cittert–Zernike theorem, the lateral degree of coherence at the sample is the normalized Fourier transform of the source intensity distribution. For a uniform circular source of diameter D the coherence radius is often estimated by the half-first zero of the Airy pattern[6],

$$\rho \approx 0.61 \frac{\lambda z_1}{D}, \quad (13)$$

with z_1 the source–sample distance. In our setup, observed from the microscope, the LED’s emitting area is approximately rectangular. When the half-first zero is used as the coherence-radius criterion, the coherence function becomes a product of sinc terms, yielding

$$\rho \approx 0.50 \frac{\lambda z_1}{D}. \quad (14)$$

In general, usable in-line holograms require temporal and spatial coherence high enough to retain the interference term and a narrowband, partially coherent source like a narrowband LED offers a good compromise.

2.2 Hologram acquisition

In simulation, we model the physical process in which an illumination field passes through a sample and then propagates a distance to the sensor. The free-space propagation is described by the angular spectrum method via one forward propagation. First of all, the sample property (sample’s transmission function) should be defined.

2.2.1 Sample definition

When light traverses the sample, the sample would have an absorption on the amplitude and cause a phase delay because of the difference of optical path. For the amplitude attenuation, according to Beer-Lambert theorem:

$$I \propto I_0 e^{-\alpha h(x,y)}, \quad (15)$$

α is the absorption index and $h(x,y)$ is the sample thickness along the path. The phase delay equals the optical-path difference times the wavenumber:

$$\phi(x,y) = k \cdot nh(x,y), \quad k = \frac{2\pi}{\lambda}. \quad (16)$$

Then an image can be read in grayscale value as the sample. It's better to normalize it as it can facilitate the calculation and give an intuitive feeling. So the object's transmission function can be written as:

$$t(x, y) = e^{-\alpha h(x, y)} e^{i\phi(x, y)}, \quad (17)$$

where $h(x, y)$ is the image's grayscale value. Here, this grayscale values can be seen as the sample thickness along the path. For example, larger value means larger thickness and hence has a larger amplitude absorption and phase delay. (a) in Figure 2 is the image used as sample and (b) is the field after the sample. This sample's transmission function is exactly what we want to reconstruct.

2.2.2 Forward propagation

I illuminate the sample with unit plane wave and given that the transmission function is already known so the field after sample can be easily got. Then the field on the sensor at distance z is obtained by propagating that field via angular spectrum method. (c) in Figure 2 is the sample's hologram.

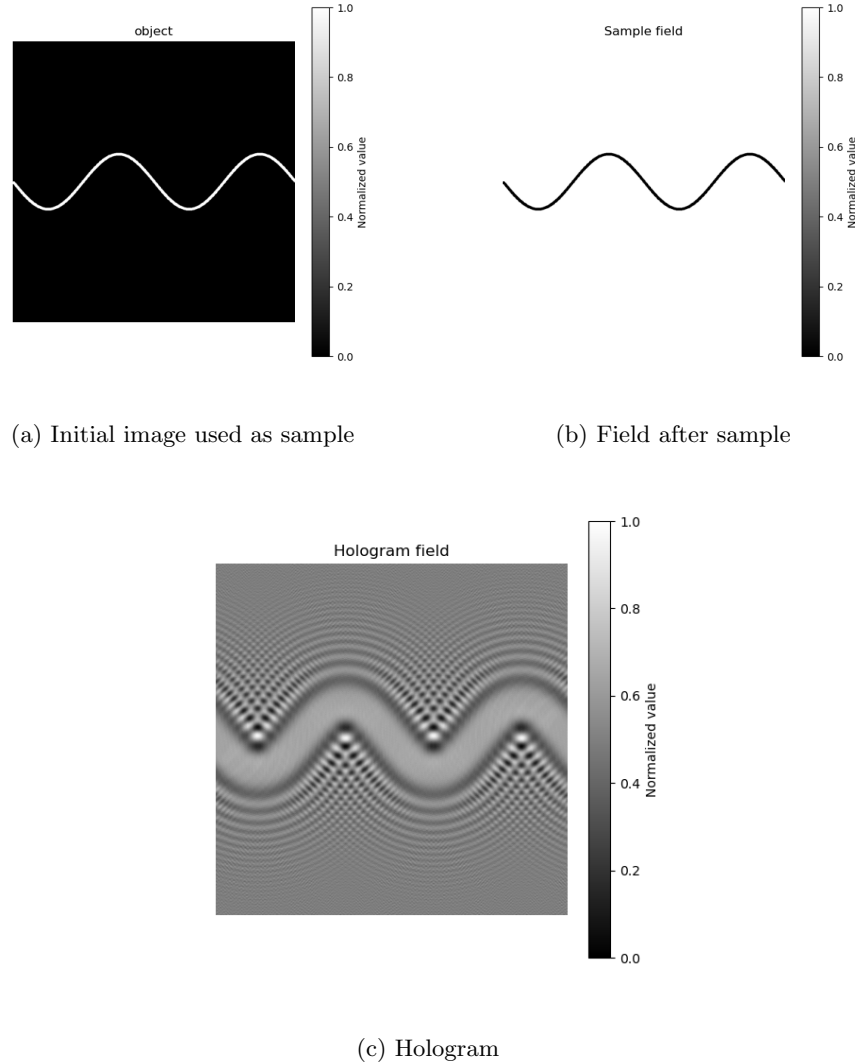


Figure 2: Sample definition and its hologram

2.3 Reconstruction of digital in-line hologram

The sensor records the hologram intensity $I(x, y)$. Hence the measured amplitude on the sensor is $A_0(x, y) = \sqrt{I(x, y)}$ while the phase is unknown. An amplitude constraint can be used within the iterative phase retrieval algorithm to reconstruct the field and suppress the twin image.

2.3.1 Phase retrieval

To eliminate the twin image, the complete wavefront should be reconstructed. However, the sensor can only record the intensity and the phase information is lost during the measurement. But the phase information somehow is converted to intensity variations for recording. Gerchberg and Saxton developed the first iterative algorithm for phase retrieval (the GS algorithm) to accurately reconstruct not only the phase but also the amplitude absorption (the transmission function) for coherent diffraction imaging (CDI).

Classical GS algorithm. The initial GS algorithm needs two intensity measurements on the sample plane and the sensor plane respectively. The two fields on the sample and sensor plane are connected by the Fourier transform. The procedure is shown below in Figure 3. a_0 and A_0 are the measured amplitudes on the sample plane and sensor plane.

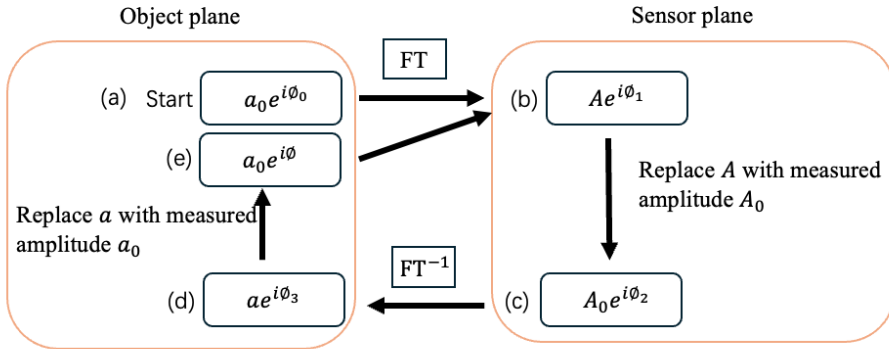


Figure 3: Schematic of GS algorithm

The scheme of the GS algorithm is: (a) It starts from the object plane U_0 with an initial guess of phase ϕ_0 . (b) The field on the sensor plane U_1 is obtained by Fourier transforming the object plane's field. (c) Then the updated sensor field U_2 is got by replacing the amplitude with the recorded A_0 . (d) After that, an inverse Fourier transform is applied to give the field on the sample plane U_3 . (e) Replace the amplitude with recorded amplitude a_0 to obtain the updated field U_4 . (f) The last step is to repeat (b) to (e). The output of this algorithm is the wavefront for both the object and sensor plane[7].

Iterative phase retrieval algorithm. However, this GS algorithm for CDI is under the condition of far field but it is not the case for the in-line holography as it is within the near field. In in-line holography, the connection between the field of sample and sensor plane is through a more complex integral transformation like the angular spectrum method. The iterative phase retrieval algorithm I used is based on the work of Tatiana Latychevskaia [8]. Different from GS algorithm, the iterative phase retrieval algorithm additionally applies a non-zero constraint on the sample plane. On the sample plane, the absorption index can be obtained from the back-propagated field. The constraint is applied when the absorption index becomes negative, as it must remain non-negative due to energy conservation. For points with a negative absorption index, the corresponding amplitude is set to 1 and the phase to 0.

The whole process of the algorithm is shown below in Figure 4: (a) Starting from the sensor plane, an initial guess of the phase is made. The initial field is given by $U_0 = A_0 \exp(i\phi_0)$, where A_0 is the measured amplitude at the sensor. (b) The field U_0 is back-propagated to the sample plane, yielding

U_1 . (c) A non-negative constraint is applied to obtain U_2 . (d) The field U_2 is forward-propagated to the sensor plane, giving U_3 . (e) The amplitude of U_3 is updated by replacing it with the measured amplitude, resulting in U_4 . (f) Steps (b)–(e) are repeated until convergence is achieved. The output is the wavefront of the hologram at the sensor.

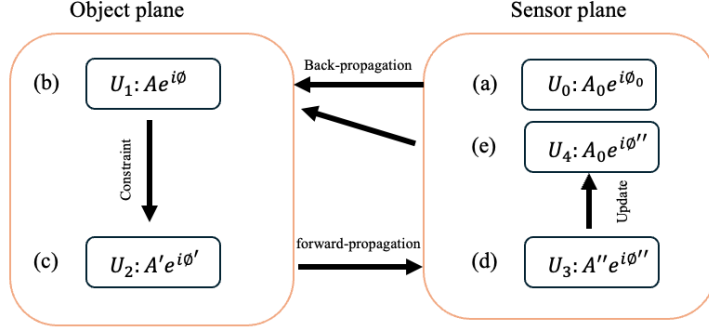


Figure 4: Schematic of iterative phase retrieval algorithm

Reconstruction from one single-shot hologram. Figure 5 shows two sets of reconstructions. Panels (a)–(c) correspond to the first set, presenting the sample, its hologram, and the reconstructed image respectively. Panels (d)–(f) show the same sequence for the second set. As can be seen, the first set is well reconstructed with SSIM = 0.93 and the second set also achieves a good reconstruction with SSIM = 0.92. However, in Figure 5(f), faint rings can be observed around the circular region. This relatively lower reconstruction quality is attributed to the properties of the sample, which will be further discussed in Section 2.5.1.

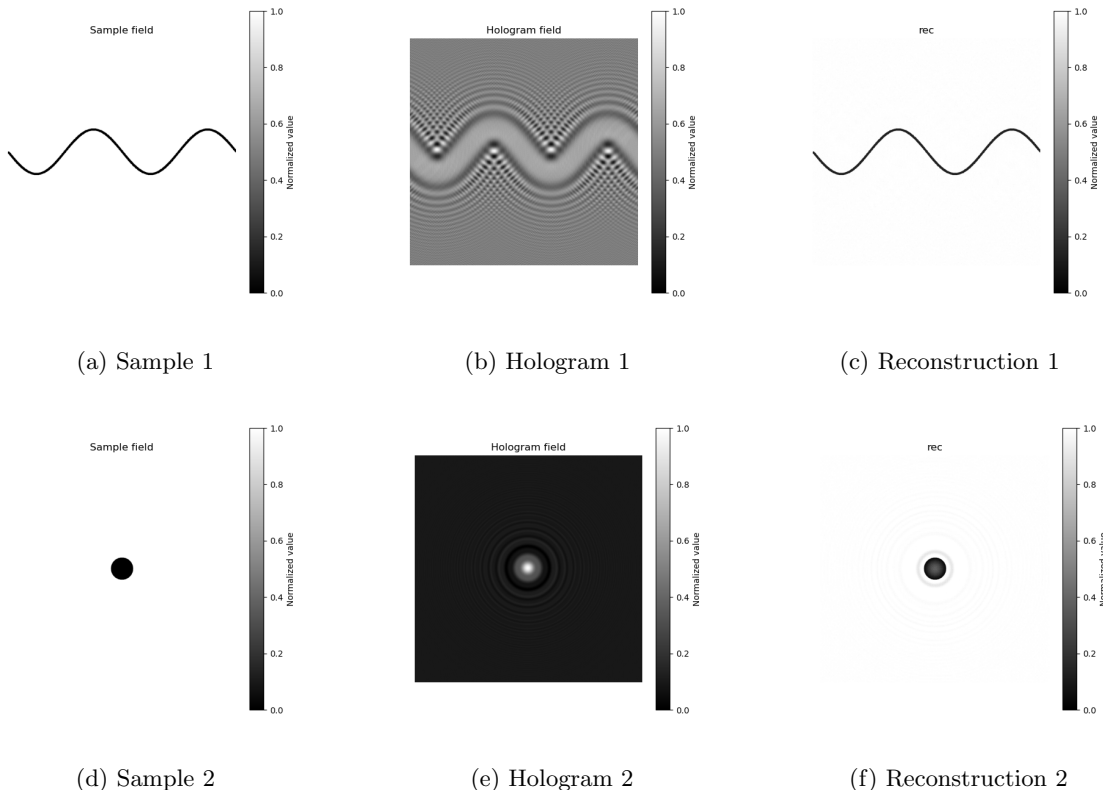


Figure 5: Reconstruction

2.4 Practical simulation

Real holograms are affected by multiple noise sources originating from both illumination and the sensor. In the simulation, I adopt a physically grounded sensor model. I model two dominant sensor noises here. Besides, not all the scattered object waves can still keep a coherence with the reference wave so a filtering effect should be considered. At last, the optical field is continuous, while the sensor can only record the discrete intensities over pixel areas. In short, these three factors should also be considered in the simulation.

2.4.1 Noise simulation

Noises are inevitable in devices. In the following simulation, I only simulate the two dominant noise in the sensor which are the dark current noise and the quantization noise and leave readout noise and PRNU/DSNU for future work.

Dark current noise. The generation of photoelectrons and thermally generated electrons is a counting process. For a fixed exposure time t , the number of electrons collected follows a Poisson distribution. Specifically, the dark signal per pixel can be modeled as

$$D \approx \text{Poisson}(\mu t), \quad (18)$$

where μ is the dark current rate. For sufficiently long exposures, it can be described by a normal distribution:

$$D \approx N(0, \sigma^2 = \mu t). \quad (19)$$

Quantization noise. Assume an n -bit sensor with 2^n levels and its range is from a to b . The maximum code value L is:

$$L = 2^n - 1. \quad (20)$$

However, the values between every two levels can't be measured. These values are rounded to the nearest level and hence the quantified value is:

$$Q(x) = \frac{\text{Round}(x \cdot L)}{L}, \quad (21)$$

with x the normalized origin signal. Then, the quantization noise ϵ is generated within this process and it equals:

$$\epsilon = Q(x) - x. \quad (22)$$

For example, let $a = 1, b = 9, n = 3$ and the real signal $x = 3.2$. First normalize the real signal with $x' = \frac{3.2-1}{9-1} = 0.275$ so the quantization value $Q = \frac{\text{round}(x'L)}{L} = 0.285$. Then the quantization error is 0.01.

Practice. For the dark current noise, it is in the scale of electron. Therefore, when adding this noise to the recorded hologram, the intensity must first be converted into electrons. After the noise is added, it should be transformed back into intensity. In contrast, quantization noise can be directly treated in intensity.

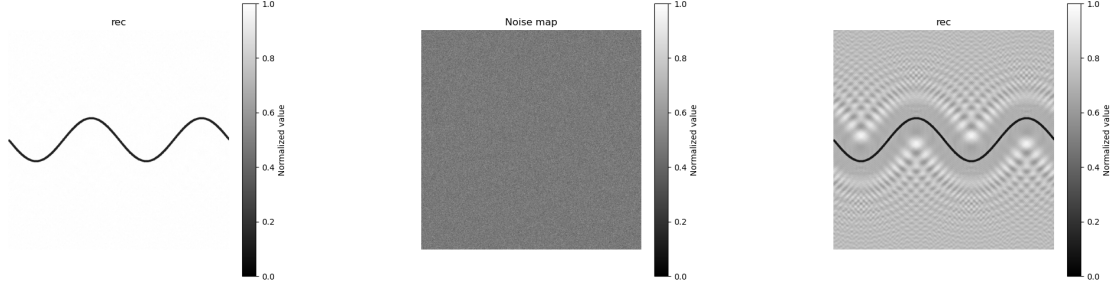
Figure 6(a) shows the reconstruction without noise, (b) presents the noise map and (c) illustrates the reconstruction with noise. As can be observed, under noisy conditions, the object in the sample can still be well reconstructed. However, artifacts appear around it. Compared with the noise-free reconstruction, the noisy reconstruction exhibits noticeable deviations.

2.4.2 Filtering effect

Physically, limited temporal and spatial coherence suppress high-angle interference fringes. However, this issue is not considered in the previous simulation.

As mentioned in Sec. 2.1.4, there are two parameters to indicate what kind of beams can keep a coherence with the reference beam. One is the coherent radius ρ on the sensor plane and another is the coherent length L_{coh} .

$$\rho \approx 0.5 \frac{\lambda z_1}{D}, \quad L_{coh} \approx \left(\frac{2 \ln 2}{\pi} \right) \frac{\lambda^2}{n \Delta \lambda}. \quad (23)$$



(a) Reconstruction without noise

(b) Noise map

(c) Reconstruction with noise

Figure 6: Reconstruction Comparison with and without Noise

In Figure 7, only the scattered waves that remain coherent with the reference wave are illustrated. The maximum scattering angle among these waves is denoted by θ_{\max} , meaning that only waves within this angle can interfere with the reference beam and form patterns on the sensor plane. This angle is determined by the smaller of the coherent radius ρ and the coherence length L_{coh} .

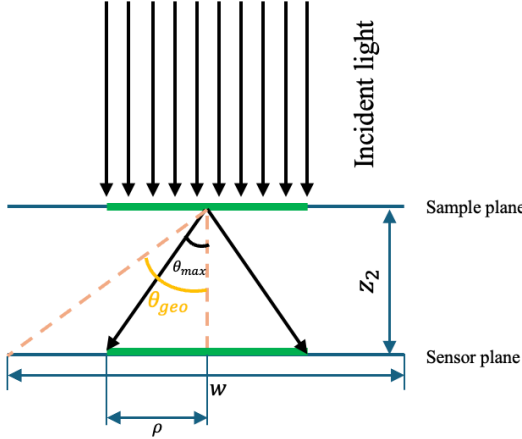


Figure 7: Scheme of light propagation

The maximum scattered angle determined by the coherent length is described as:

$$\theta_1 = \arccos \left(\frac{z_2}{z_2 + L_{coh}} \right), \quad (24)$$

with z_2 the sample-sensor distance. For in-line holography, the sample-sensor distance z_2 usually is very small ($\leq 1\text{mm}$) and so is the scattered angle ($< 1^\circ$). As a result, the coherent radius remains nearly unchanged on the sensor plane. So the maximum scattered angle determined by the coherent radius is calculated as:

$$\theta_2 = \arctan \frac{\rho}{z_2} = \arctan \frac{0.5\lambda z_1/D}{z_2}, \quad (25)$$

where z_1 is the illumination-sample distance. Hence, the maximum scattered angle is:

$$\theta_{\max} = \min\{\theta_1, \theta_2\}. \quad (26)$$

However, a special case arises when the maximum scattering angle θ_{\max} exceeds the maximum geometrical half-angle of the sensor, denoted as θ_{geo} :

$$\theta_{geo} = \arctan \left(\frac{w/2}{z_2} \right), \quad (27)$$

where w is the width of the sensor. In this case, the effective scattering angle is limited by θ_{geo} . Consequently, the final expression for the maximum scattering angle becomes

$$\theta_{\max} = \min\{\theta_1, \theta_2, \theta_{\text{geo}}\}. \quad (28)$$

Next step is to filter the waves that are not within this angle. This can be done directly by low-pass filtering during the forward propagation. The frequency of the wave equals to:

$$f = \frac{k}{2\pi}, \quad (29)$$

then its frequency is:

$$f_x = \frac{k_x}{2\pi} = \frac{k \sin \theta \cos \phi}{2\pi} = \frac{\sin \theta \cos \phi}{\lambda}, \quad f_y = \frac{\sin \theta \sin \phi}{\lambda}. \quad (30)$$

ϕ represents the azimuth which is defined as the angle of the wave vector direction in the transverse plane. So the maximum value of these lateral frequencies is:

$$f = \sqrt{f_x^2 + f_y^2} = \frac{\sin \theta}{\lambda}, \quad f_{\max} = \frac{\sin \theta_{\max}}{\lambda}. \quad (31)$$

A new constraint can be added to the free space transfer function to filter these waves during the forward propagation which is:

$$f_x^2 + f_y^2 \leq f_{\max}^2. \quad (32)$$

This treatment approximates the effect of partial coherence by limiting the lateral k-vectors that produce visible interference with the on-axis reference wave. Figure 8.(a) is the intial reconstruction and (b) is the reconstruction after filtering.

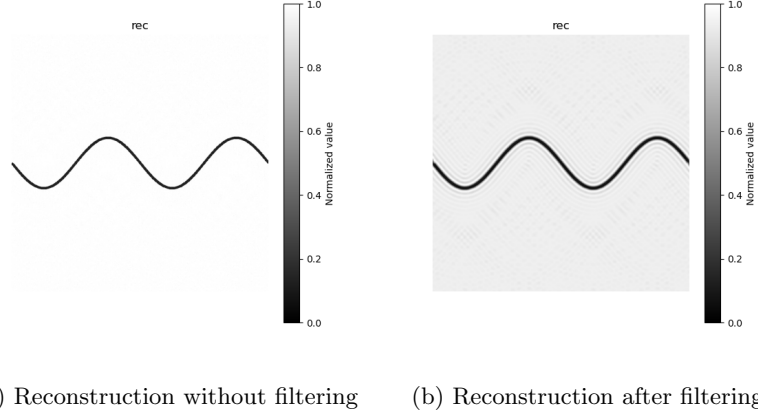


Figure 8: Reconstruction Comparison with and without filtering

2.4.3 Sampling simulation

In reality, the optical field $U(x, y, z)$ is continuous, whereas an image sensor returns a discrete array. In simulation I compute the hologram on a finer grid and then downsample it to the sensor grid.

Assume the field of view (FOV) is the same on both the sample and sensor plane as in in-line holography, the FOV is nearly the same with the sample area. Its width is L in both x and y . Let the simulated hologram be an $M \times M$ array and the sensor have $N \times N$ pixels with $M > N$. The decimation factor s is:

$$s = \frac{M}{N} (> 1), \quad (33)$$

to better simulate, this factor should better be an integer. For now, I ignore the pixel integration effect at this time and the sensor sampled values are obtained by selecting every s -th value on the fine grid (the complete hologram field):

$$I_{\text{sensor}}[m, n] = I_{\text{hologram}}[ms, ns], \quad m, n = 0, \dots, N - 1. \quad (34)$$

In Figure 8, (a) is the complete hologram field and (c) is the sampled hologram field. (b) is the reconstruction of the complete hologram and (d) is the reconstruction of the sampled field. In this example, the decimation factor is 4 and as can be seen, the sample field is reconstructed well but with lower sharpness. To be noted that to avoid aliasing, it's better to apply a low-pass filter with bandwidth equals to $\frac{1}{2\Delta x_{sensor}} = \frac{N}{2L}$.

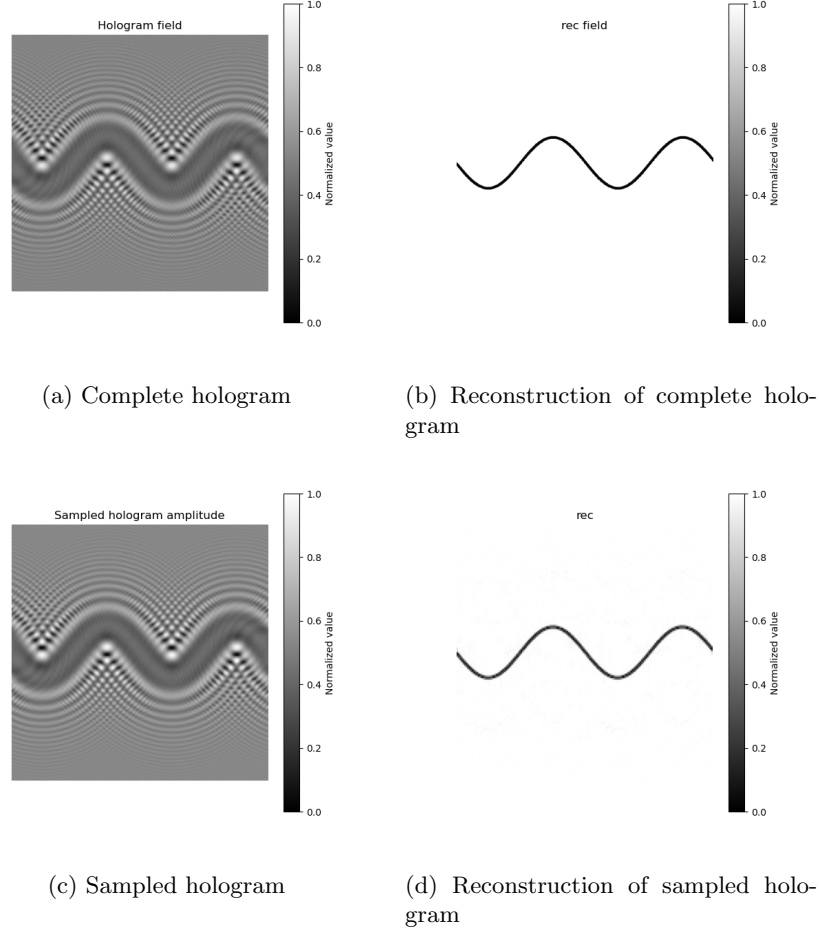


Figure 9: Reconstruction comparison with and without sampling

Pixel integration effect. In the mathematical model above, I considered the sampling process as "point sampling" (taking a value at a specific pixel). In practice, however, the operation of an image sensor is more complex. Instead of capturing an instantaneous value at one point, it integrates the optical signal over its finite pixel area and the exposure duration.

If the brightness remains unchanged during exposure, the integration on time becomes a constant. Hence, the pixel value is the integration over its pixel area:

$$s = \iint U(x, y) \operatorname{rect}\left(\frac{x - x_m}{\Delta}, \frac{y - y_n}{\Delta}\right) dx dy \quad (35)$$

where $U(x, y)$ is the hologram intensity distribution over this pixel, Δ is the width of the pixel and (x_m, y_n) the center coordinate of this pixel. To simplify the calculation, we make a Fourier transform to convert a convolution to a multiplication in Fourier domain:

$$\mathcal{F}(s) = A(x, y) \times \mathcal{F} \left\{ \operatorname{rect}\left(\frac{x - x_m}{\Delta}, \frac{y - y_n}{\Delta}\right) \right\} = A(x, y) \times \operatorname{sinc}(f_x \Delta) \operatorname{sinc}(f_y \Delta), \quad (36)$$

$A(x, y)$ is the Fourier transform of $U(x, y)$. Then by inverse Fourier transforming, we can obtain s :

$$s = \mathcal{F}^{-1} \{A(x, y) \times \text{sinc}(f_x \Delta) \text{sinc}(f_y \Delta)\}. \quad (37)$$

This part is based on material from a Stanford lecture slide and it is included in the Git repository. Figure 10.(a) is the complete hologram field and (c) is the sampled hologram field by pixel integration. (b) is the reconstruction of the complete hologram and (d) is the reconstruction of the sampled field.

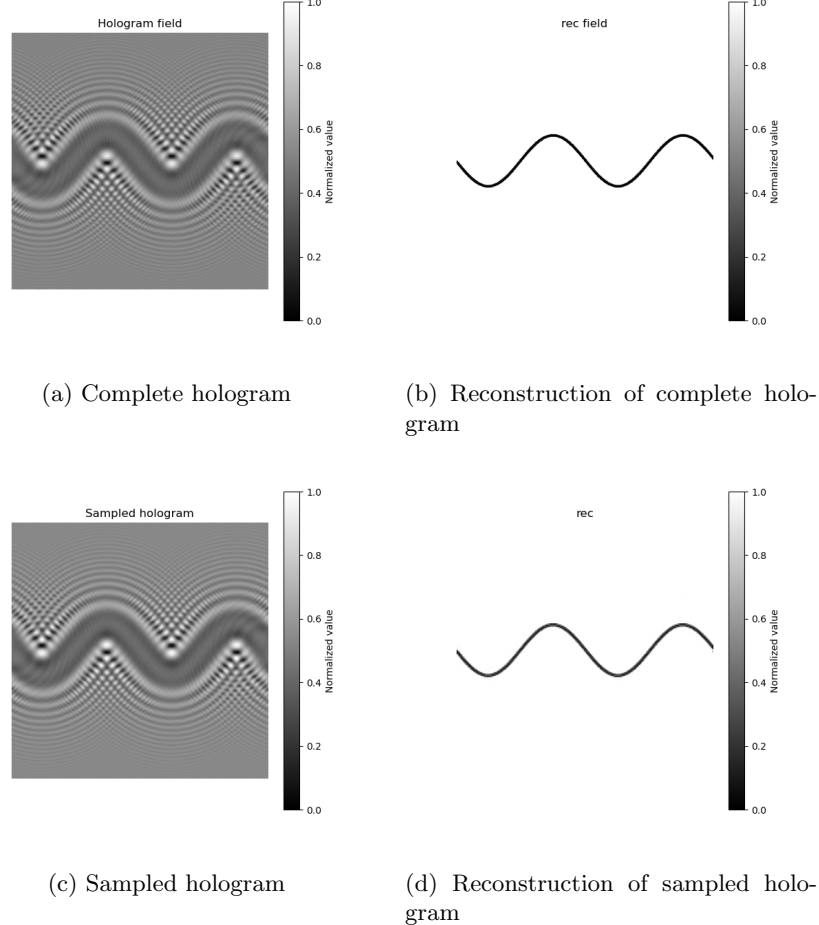


Figure 10: Reconstruction comparison with and without sampling(Pixel integration)

2.4.4 Simulation with all the factors considered

When all the above factors are taken into account in the simulation, the reconstruction result is shown in Figure 11 with (a) the initial reconstruction and (b) the reconstruction with all the factors. Still the object can be reconstructed with a good quality but with some artifacts around it.

2.5 Supplementary tests

After establishing the simulation framework, we can predict the reconstruction resolution. In particular, I examine its dependence on the sample–sensor distance z_2 and the sensor pixel size Δ . This prediction is made under noiseless conditions, as the noise characteristics of the equipment are difficult to determine: they are not specified in the manuals and may vary across devices. Moreover, not all samples are suitable for digital in-line holography, and the suitability criteria will be discussed below.

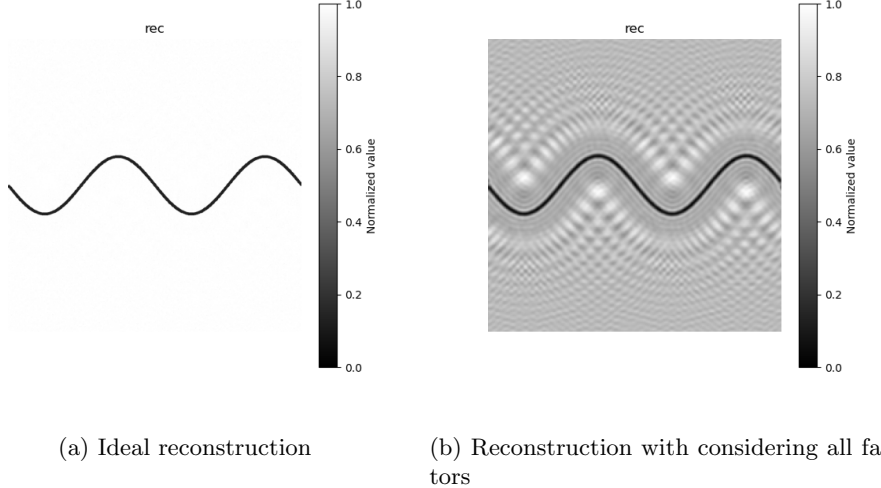


Figure 11: Reconstruction comparison with all factors considered

2.5.1 Simulation validation of the resolution bound

The half-pitch resolution of the system is given by

$$\Delta x = \frac{\lambda}{2NA} = \frac{\lambda}{2n \sin \theta_{\max}}, \quad (38)$$

where λ is the wavelength, n is the refractive index, and θ_{\max} denotes the maximum scattering angle. As mentioned in Section 2.4.2, θ_{\max} represents the effective maximum scattering angle that can still maintain coherence with the reference wave. It is constrained by temporal coherence, spatial coherence, and the maximum geometrical half-angle

$$\theta_{\max} = \min(\theta_1, \theta_2, \theta_{\text{geo}}). \quad (39)$$

θ_1 , θ_2 and θ_{geo} are functions of the sample–sensor distance z_2 . However, if we don't introduce multiple measurements, the best achievable resolution is limited by the sensor's pitch size. When sampling by a pixel grid of pitch Δ imposes a Nyquist limit

$$f_N = \frac{1}{2\Delta}.$$

The smallest resolvable period is $P_{\min} = 1/f_N = 2\Delta$. Hence the best half-pitch resolution is

$$\Delta x_{\text{best}} = \frac{P_{\min}}{2} = \Delta. \quad (40)$$

If the lateral spatial frequencies present at the sensor exceed f_N , aliasing folds them into lower frequencies and damages the reconstruction.

In this test, the actual parameters of the narrowband LED to be used is applied with a bandwidth of 30nm and a lateral size of 50 μm . The LED–sample distance z_1 is set to 20cm which is achievable in practice. The width of the field is 240 μm . Two tests are done with their pitch size 1 μm and 1.6 μm . In each test, the sample–sensor distance z_2 was varied from 1 mm to 3 mm. To verify the reconstruction resolution, gratings with different periods were generated for testing and the resolution was determined from their reconstructions.

In Figure 12, the curves represent the theoretical resolution as a function of z_2 , while the red crosses indicate the experimental results. As can be observed, the two curves are the same as they are all coherence-limited (the sampling floor Δ and the FOV limit are looser), hence the two theoretical curves coincide for the two pixel pitches. The trend of the test results basically aligns with the curve but not perfectly because first it is a little bit hard to quantify the reconstruction resolution so there

would be errors during resolution determination. Second, the red crosses is always slightly larger than the predicted value this is because the finite pixel area further attenuates high frequencies. Besides, comparing Fig. 12(b) to Fig. 12(a), the $1.6\text{ }\mu\text{m}$ -pitch sensor shows a slightly worse resolution at small z_2 . This is also because of the pixel integration effect as the MTF first zero occurs at a lower frequency with a larger pixel pitch, $f_0 = 1/\Delta$ (i.e., $1/1.6 < 1/1.0 \text{ }\mu\text{m}^{-1}$) so attenuation starts earlier.

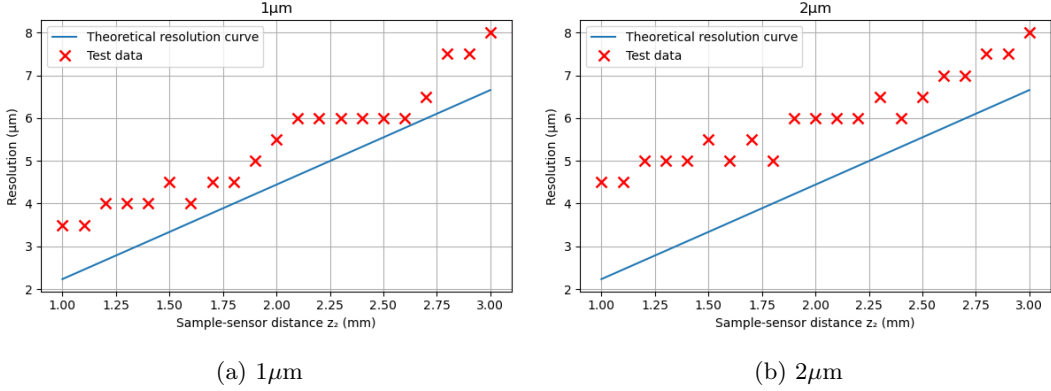


Figure 12: Theoretical resolution curve vs The test results

2.5.2 Criteria of suitable sample for LIHM

For LIHM, it is well known that it is not suitable for dense samples except that we introduce multiple measurements like multi- z_2 recording. Beside this, actually there are some other requirements for a sample as well. In this part, I mainly take reference from Tatiana's work in 2024 [9].

First and foremost, the operating regime for LIHM should be clarified. As mentioned above in Section 2.3.1, unlike CDI, it works in the Fresnel regime (near field) and the reconstruction is based on the recorded in-line hologram. An in-line hologram forms when a strong reference wave (the part of the beam that does not interact with the object) interferes with a weaker object wave (the part that does interact). In practice this means the object must occupy only a small fraction of the illuminated field so that the reference wave remains strong.

We define a sparsity metric here:

$$\kappa = \frac{\text{object's projected area}}{\text{illuminated field (or detector FOV) area}} \in (0, 1).$$

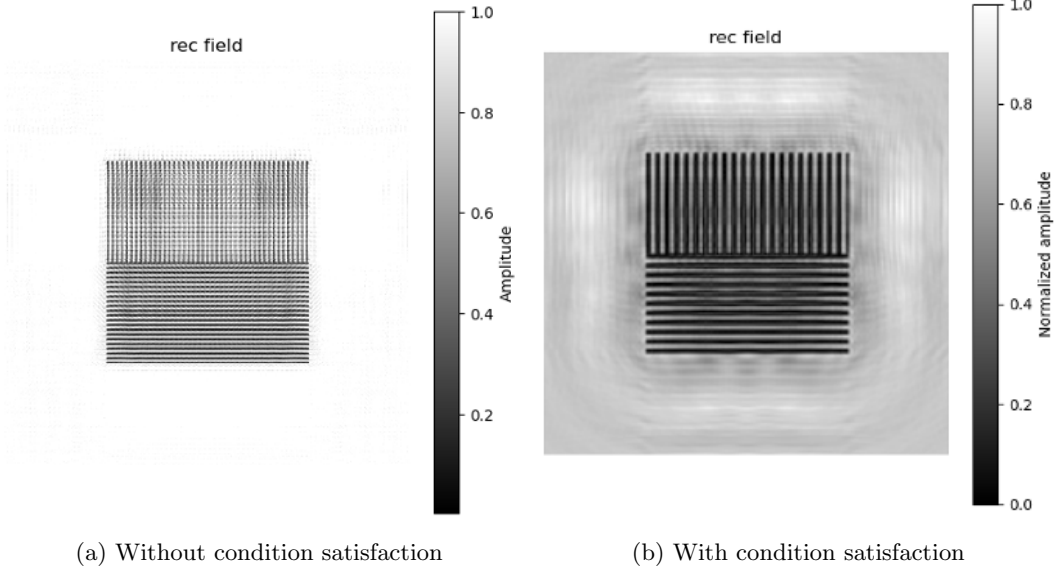
Back-propagation (no IPR) : If the iterative phase retrieval algorithm is not applied and the reconstruction only depends on the backpropagation, then there is a common safe rule that we need to satisfy $\kappa \leq 1\%$ to ensure the background in the reconstruction is nearly flat and twin image artifacts remain low enough for reliable recognition.

When κ grows, the unavoidable twin-image and higher-order terms superimpose more strongly on the back-propagation result, preventing quantitative retrieval of absorption/phase even if the object is still recognizable. Thus, back-propagation is best reserved for small κ and qualitative analysis.

With iterative phase retrieval algorithm If we apply IPR algorithm on the hologram, the admissible object size is the same as in coherent diffraction imaging (CDI): in each dimension, the object's extent must be less than half of the probed field. The oversampling ratio σ must satisfy:

$$\sigma = N/N_0 > 2 \quad (41)$$

Under this condition, IPR removes the twin image and enables quantitatively accurate amplitude and phase reconstructions for amplitude-only, phase-only, or mixed objects. Figure 13 shows a reconstruction comparison: (a) and (b) are both the reconstruction of the same grating with the same parameters; the only different thing is their oversampling ratio. (a) doesn't satisfy the requirement while (b) meet that condition and it is cropped for easier viewing. Obviously, (b) has a much better reconstruction compared with (a).



(a) Without condition satisfaction

(b) With condition satisfaction

Figure 13: Comparison of reconstruction with and without condition satisfaction

Besides, J.R. Fienup noted that the central symmetrical sample is not quite suitable for reconstruction. During the iteration process, the Fourier domain can be divided into two complementary regions: in one region the phase converges to the true image, while in the other it converges to the twin image. In the spatial domain, this results in a superposition of the true image and the twin image, producing ghost artifacts with strong symmetry. Such stagnation is usually persistent and cannot be easily eliminated by further iterations or small perturbations.

In-line holography inherently suffers from a conjugate twin image, which is symmetric with respect to the origin of the object plane. When the sample itself is approximately central symmetric, the geometrical and intensity symmetry further facilitates the matching and overlap between the true and twin images, making iterative phase retrieval (IPR) more prone to fall into this type of 'partitioned stagnation'[10].

So that's why in Section 2.3.1, the circular object's reconstruction has artifacts around it even it's under the ideal case without considering noise, sampling and filtering effect.

3 Setup construction

The setup is relatively simple as illustrated in Figure 14. Component (a) is a U3-3060CP-M-GL Rev.2 sensor with $5.86\mu\text{m}$ pixel size. I can't get a short sample-sensor distance z_2 because of its cover (nearly 7cm long). Component (b) is a narrowband LED light source with a bandwidth of approximately 30nm and a lateral emission width of about $50\mu\text{m}$. Component (c) is the sample holder platform. All components are mounted on an adjustable support, and the platform beneath the LED is also height-adjustable. The target used for test is a USAF 1951 1x target.

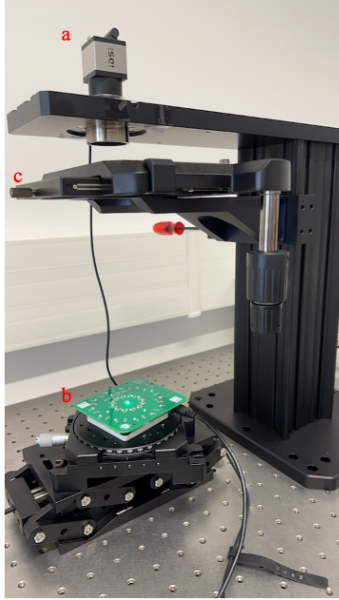


Figure 14: Setup

4 Implementation details with the setup

Autofocus algorithm. The iterative phase retrieval algorithm requires an accurate sample–sensor distance z_2 . However, due to the presence of the protective glass and cover, it is difficult to measure this distance precisely. Fortunately, Wei Luo proposes an algorithmic solution in their work.

To estimate the sample-sensor distance, we can back-propagate the hologram to different planes. In each plane, this autofocus algorithm uses Sobel operator to evaluate the sharpness of the resulting image. This sharpness is defined as the variance of the gradient of the image. As a result, the plane with the highest sharpness is selected as the object plane [2]. In practice, this method works properly.

Figure 15 is a hologram taken by this setup. The sample-sensor distance is obtained by this autofocus algorithm and Figure 16 is its reconstruction.

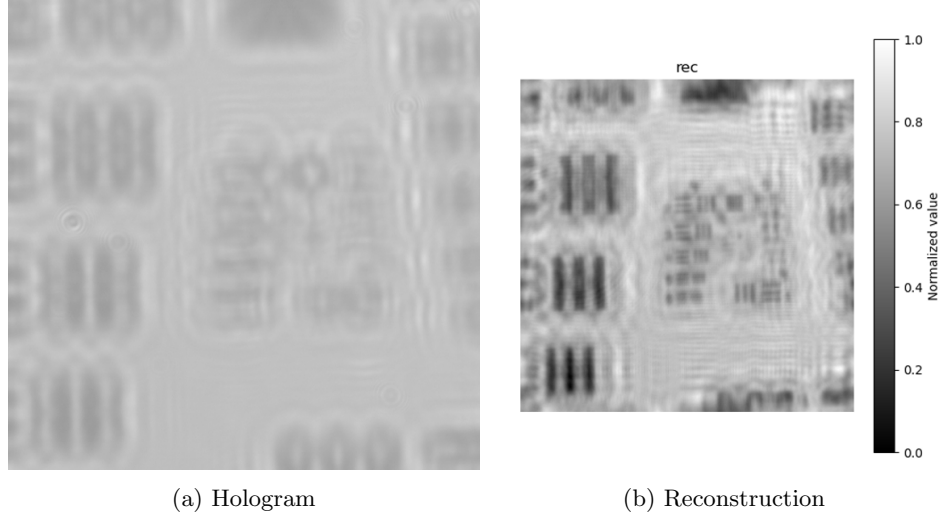


Figure 15: Reconstruction with the estimated z_2

Object support. Applying an object support allegedly can improve reconstruction quality by suppressing out-of-support artifacts and stabilizing phase retrieval [11]. I therefore add a support mask $S(x, y)$ that marks where the object actually is. After flat-field normalization, the empty background

has amplitude ≈ 1 . Hence, object regions coincide with where the amplitude deviates from 1. My update follows three steps:

First, the deviation from the background is measured. Given the object-plane field $U(x, y)$ obtained by back-propagating the measured hologram, the amplitude is defined as

$$A(x, y) = |U(x, y)|,$$

which is normalized such that the background is approximately unity. The deviation map is then computed as

$$D(x, y) = |A(x, y) - 1|.$$

Second, Gaussian smoothing is applied to suppress noise, yielding

$$\tilde{D}(x, y) = (G_\sigma * D)(x, y),$$

where G_σ denotes a Gaussian kernel with standard deviation σ .

Third, I apply a threshold to obtain S (the object region). To binarize the smoothed map, I use a scale-free relative threshold T :

$$T = \alpha \cdot \max \tilde{D}, \quad S(x, y) = \mathbf{1}\{\tilde{D}(x, y) > T\}.$$

Here $\alpha \in (0, 1)$ controls the tightness of the support: larger α yields a more conservative (smaller) support, while smaller α yields a looser (larger) support. $\tilde{D}(x, y) > T$ represents the object area as the object region has a larger deviation compared with the background. We can increase α if background leakage is observed and decrease α if weak features are eroded. A larger σ merges speckles but may oversmooth thin structures, whereas a smaller σ preserves details but is more sensitive to noise.

However, no obvious improvement is achieved with the optimum support parameter $\alpha = 0.2$. If we continue slightly tightening α to 0.23, the reconstruction quality is degraded. Figure 17(a) shows the reconstruction of the hologram in Figure 15 with $\alpha = 0.2$ and as can be seen, the reconstruction improvement is not observed. While Figure 17(b) presents the reconstruction with $\alpha = 0.23$. To avoid potential problems, the support constraint was abandoned in the following work as barely no improvement is observed.

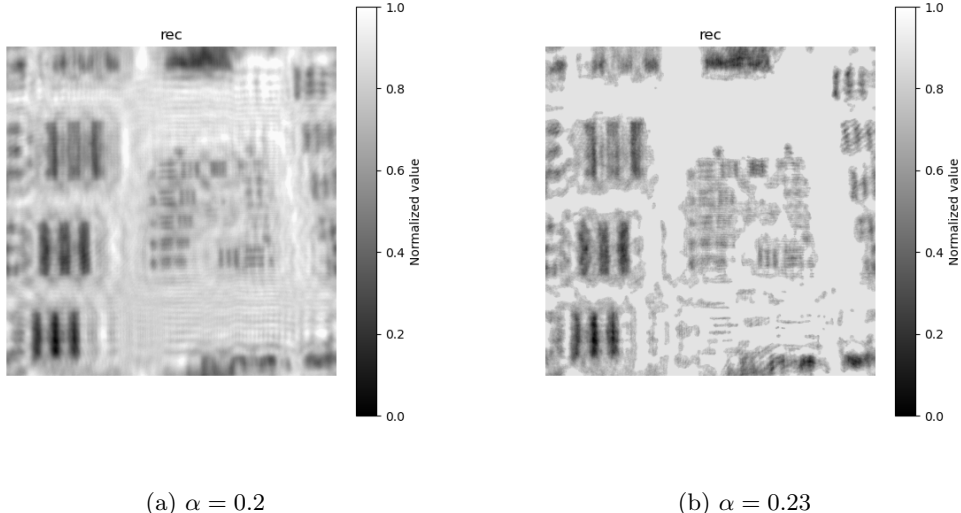


Figure 16: Reconstruction with support constraint

5 Experiments

I did some experiments to verify the simulation framework. The USAF target is not sufficiently sensitive to reflect fine changes in resolution, since adjacent elements differ by several micrometers.

For example, there is a $3\ \mu\text{m}$ gap between group 4 element 2 ($27.8\ \mu\text{m}$ resolution) and group 4 element 3 ($24.8\ \mu\text{m}$). As a result, the target cannot capture resolution variations between $24.8\ \mu\text{m}$ and $27.8\ \mu\text{m}$. So based on the varying degrees of blurriness observed within the same element, I assign different values to give a more intuitive resolution change.

The parameters are shown in the table below. The curve in Figure 17 represents the predicted value (without noise) and the red crosses represent the real test. Please excuse the test distribution as this device is difficult to modify the sample-sensor distance precisely. To be noted that, there's a small change in my framework because the sample-sensor distance is not small enough to apply the approximation. So the coherent radius should be changed to:

$$\rho = 0.5 \frac{\lambda(z_1 + z_2)}{D}. \quad (42)$$

The temporal coherence is always the limitation for reconstruction resolution. With smaller sample-sensor distance, we can have a larger scattering angle (temporal coherence limited) and hence a higher resolution. The tests result nearly align with the framework just with an acceptable difference as the noise is not considered in the framework.

Table 1: Parameters of first test

Parameter	Value
Wavelength λ	525nm
Bandwidth $\Delta\lambda$	30nm
LED lateral size D	50 μm
Pixel size Δ	5.86 μm
FOV	3516 $\mu\text{m} \times 3516\mu\text{m}$
LED-sample distance z_1	20cm

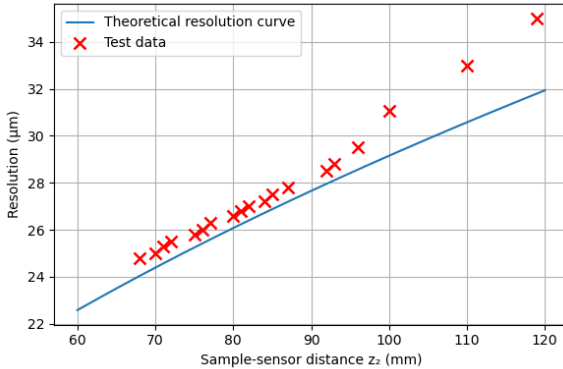


Figure 17: Test result

HDR. To improve the SNR of weak interference fringes, I record the same field with multiple exposure times and fuse them in a high-dynamic-range (HDR) image. This can lift faint fringes above the read noise. During the process of HDR synthesis, I apply triangular weight to down-weight unreliable measurements. Very dark pixels are dominated by noise and the over-exposed pixel is not useful. We want to use the pixels with moderate values so they should be given a high weight.

Figure 18.(a) is the normal hologram and (c) is its reconstruction. (b) is the HDR hologram and (d) is HDR hologram's reconstruction. Figure 19 is the two reconstruction's difference map. As can be seen, their reconstruction is basically the same. I think this can be attributed to the fact that the normal hologram is free from saturation at the mean time the dark fringes are above the noise level. As a result, HDR reconstruction only yields marginal improvements in linearity and SNR stability.

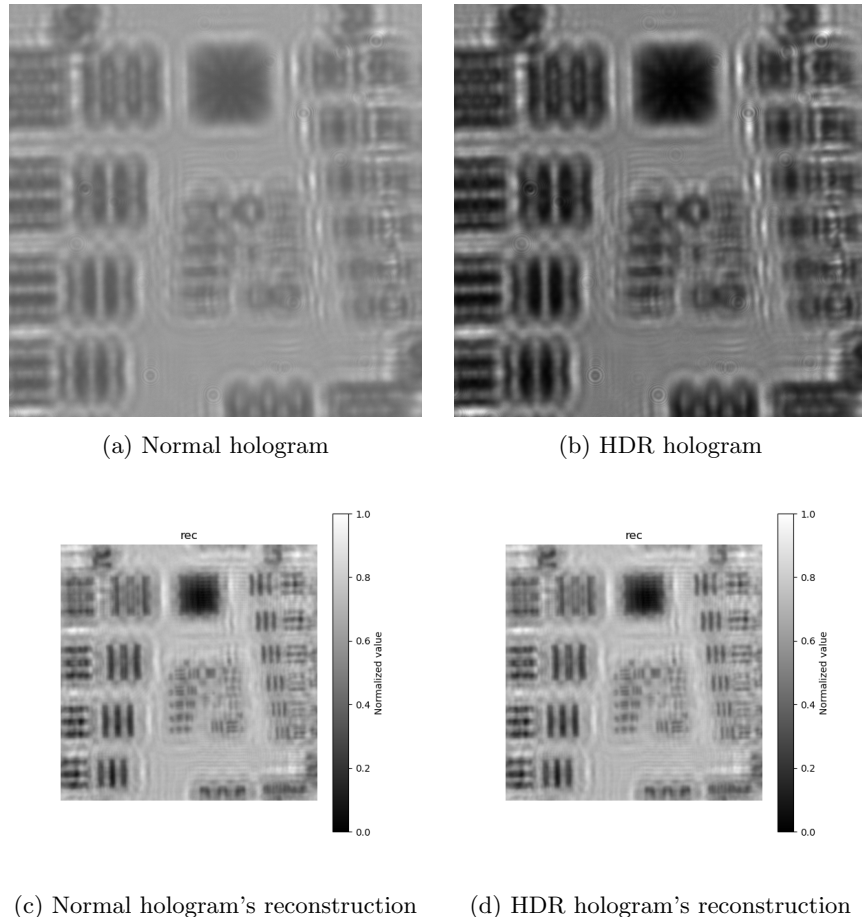


Figure 18: Reconstruction comparison with HDR image

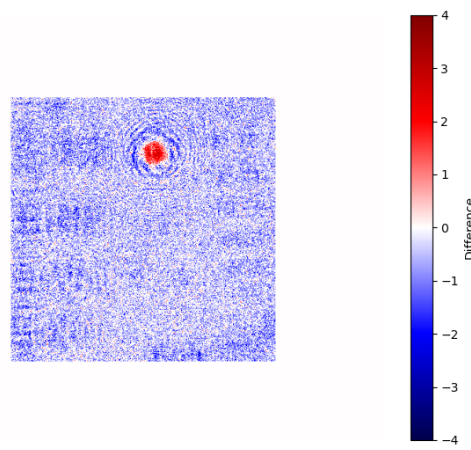


Figure 19: Difference map

6 Acknowledgement

The above summarizes my recent work. I sincerely appreciate your reading and patience. Here, I would like to express my heartfelt gratitude to my supervisor Prof.Yaneck Gottesman's invaluable support and patient guidance. Throughout my study, I often encountered confusion and sometimes

found it difficult to understand at once but he always took the time to explain with patience and clarity. Thanks to him I can really feel how much I have improved over the past year. Beyond academic matters, my dear and respected supervisor also provided encouragement and advice when I faced personal difficulties and was always willing to engage in open conversations with us. I am truly touched and deeply grateful and words cannot fully convey my appreciation. He's truly my favorite teacher ever!

7 Paper collection

The following papers are essential for studying lensless in-line holography. They're arranged in the order I would read them and grouped into three sections:

1. Introduction, Development & Key Technologies of Lensless In-line Holography
2. Tutorials on Iterative Phase-Retrieval Algorithms and Twin Image Processing
3. Reconstruction-Resolution Analysis and Prediction

7.1 Introduction, Development & Key Technologies of lensless in-line holography

1. *Lensless Imaging and Sensing*[1]

They present an introduction to lensless imaging approaches including shadow imaging, fluorescence imaging and digital holography. They introduce the angular spectrum method for modeling wave propagation and the way to calculate in-line holography's theoretical resolution limits. Also, pixel super-resolution and multi-height method is mentioned.

2. *Synthetic aperture-based on-chip microscopy*[2]

This paper introduces a lensless imaging technique achieving a large effective numerical aperture of 1.4—corresponding to a 250 nm half-pitch resolution. By combining multi-angle illumination with pixel-super-resolution and then applying a synthetic-aperture phase-retrieval algorithm, they reconstruct sub-micrometer details without any conventional optics.

3. *Lens-free optical tomographic microscope with a large imaging volume on a chip*[12]

This paper introduces a compact, lensless optical tomography system that employs dual-axis, multi-angle illumination combined with pixel super-resolution to achieve a 15mm^3 imaging volume and $< 1\mu\text{m}$ lateral resolution and $< 3\mu\text{m}$ z-axial resolution.

4. *On-Chip Biomedical Imaging*[4]

This paper gives reviews on contact shadow imaging, lensfree holographic microscopy, lensless optical tomography and on-chip fluorescence. Also their operating principles, implementation strategies and key applications in compact, cost-effective lab-on-a-chip diagnostics are outlined.

5. *Sparsity-based multi-height phase recovery in holographic microscopy*[13]

Normal in-line holography is not suitable for dense sample unless multiple measurement is applied like multi-height recording and multi-angle illumination. This paper introduces a wavelet-domain sparsity constraint during phase retrieval, enabling accurate reconstruction of dense specimens from just two in-line holograms.

6. *Maskless imaging of dense samples using pixel super-resolution based multi-height lensfree onchip microscopy*[3]

This paper gives very detailed information on pixel super-resolution based multi-height in-line holographic imaging.

7. *Lensfree on-chip microscopy over a wide field of-view using pixel super-resolution*[14]

The multi-angle illumination scheme presented in Orzcan's *Synthetic aperture-based on-chip microscopy* is from this paper and this paper explains the theoretical foundations and every processing step more detailly.

8. *Digital in-line holography for biological applications*[15]

This paper provides a comprehensive explanation on in-line holography's principles, structure, and resolution limits. It also presents a good way to test this lensless microscope.

9. *Digital in-line holographic microscopy*[16]

It is worth noting in this paper that they use Kirchhoff–Helmholtz transform without approximation to avoid resolution and artifact issues caused by on-axis approximation.

10. *High-Precision Lensless Microscope on a Chip Based on In-Line Holographic Imaging*[11]

Aside from introduction on in-line holography, this paper gives instructions on setup construction, background noise removal and image quality evaluation.

7.2 Tutorials on Iterative Phase-Retrieval Algorithms and twin image processing

1. *Iterative phase retrieval for digital holography*[8]

This paper gives an detailed introduction to the theory of in-line holography and provides a comprehensive tutorial on Gerchberg–Saxton–based iterative phase retrieval algorithm. Wave propagation (via Huygens–Fresnel and angular-spectrum methods), hologram recording and constraints on object and sensor plane are discussed in detail. Besides, IPR reconstruction with multi- z_2 (sample-sensor distance) is mentioned at the last part of the paper.

2. *Practical algorithms for simulation and reconstruction of digital in-line holograms*[17]

It gives two iterative phase retrieval algorithm frameworks for plane wave and spherical wave. Detailed derivations are provided for the Fresnel approximation, angular spectrum method, and theoretical resolution for each framework.

3. *Understanding the twin-image problem in phase retrieval*[10]

In this paper, the cause of twin images is discussed in great details and they provide a way to detect twin images in the reconstruction image. Also, they propose strategies to eliminate twin.

4. *Solution to the Twin Image Problem in Holography*[18]

The author introduced a new non-negative constraint on the sample plane during the reconstruction iterations and the twin image problem is successfully avoided.

5. *Iterative algorithms for twin-image elimination in in-line holography using finite-support constraints*[19]

In this paper, they apply the support area constraint to avoid twin image problems and they discuss about the convergence properties about this iterative phase retrieval algorithm.

6. *Phase-retrieval stagnation problems and solutions*[20]

The phase retrieval algorithm might be trapped into the local minimums. This paper gives explanation on this stagnation problem and also presents several solutions to it.

7. *Phase retrieval algorithms: a comparison*[21]

This paper gives introduction to the error-reduction algorithm, steepest-descent method, input-output algorithm and hybrid input-output algorithm. They made a comparison between these searching methods and presented the different properties of these algorithms.

8. *Reconstruction of an object from the modulus of its Fourier transform*[22]

As mentioned above this paper, there are error-reduction algorithm, input-output algorithm and hybrid input-output algorithm aside from the IPR algorithm. This paper provides detailed information on these three kinds of searching methods.

9. *Criteria for objects suitable for reconstruction from holograms and diffraction patterns*[9]

They investigated criteria for sample suitability for in-line holographic imaging and iterative phase retrieval. After adjusting my sample's properties according to this paper's findings, I observed a huge improvement in reconstruction quality.

7.3 Reconstruction-Resolution Analysis and Prediction

1. *Lensless In-Line Holographic Microscopy With Light Source of Low Spatio-Temporal Coherence*[23]

This paper introduces a very interesting way for the in-line hologram reconstruction. They decompose unknown large-size convolution kernels (128×128) into small-size light source-specific kernels (9×9) and known light source-independent kernels. Then they introduce upper bound constraints into the Richardson–Lucy deconvolution during the reconstruction stage to suppress noise overfitting and ringing artifacts. They achieved better resolutions compared with traditional angular spectrum method.

2. *Coherence-resolution relationship in holographic and coherent diffractive imaging*[24]

This paper mainly investigates the influence of system spatial coherence on the reconstruction resolution of a near-field hologram and CDI.

3. *Aliasing, coherence, and resolution in a lensless holographic microscope*[25]

This paper derives the aliasing-free criteria for in-line holographic imaging and proposes strategies to modify the system's spatial and temporal coherence for optimal reconstruction. However, since their setup relies on single-mode fiber coupling to achieve full spatial coherence, the results aren't directly applicable to our configuration but still worth reading.

4. *Color digital lensless holographic microscopy: laser versus LED illumination*[26]

They make a comparison between reconstructions with a laser and a LED. This paper gives us intuitive insight into how different coherence properties impact the results.

5. *Noise reduction in digital lensless holographic microscopy by engineering the light from a light-emitting diode*[27]

This paper employs a bandwidth-limited LED with pinhole filtering to substitute for the laser in in-line holography, but since our setup avoids the use of a pinhole purposely, the approach isn't directly applicable to our system.

6. *Spatial and temporal coherence effects in interference microscopy and full-field optical coherence tomography*[28]

This paper compares how a light source's temporal coherence (its spectrum) and spatial coherence (beam focus) each affect image resolution and contrast in interference microscopy and full-field OCT. It's worth reading but still can't apply their conclusion in our setup.

7. *Resolution Analysis in a Lens-Free On-Chip Digital Holographic Microscope*[29]

In this paper, the research on factors that influence the lensless in-line holography was done. There are five factors which are the sample-sensor distance z_2 , system's temporal coherence, system's spatial coherence, sensor's pixel size and the FOV used for reconstruction. Their influences on the reconstruction resolution are independent with each other and hence we can discuss their limited resolution separately. The final resolution is determined by the largest value of them.

References

- [1] Aydogan Ozcan and Euan McLeod. Lensless imaging and sensing. *Annual review of biomedical engineering*, 18(1):77–102, 2016.
- [2] Wei Luo, Alon Greenbaum, Yibo Zhang, and Aydogan Ozcan. Synthetic aperture-based on-chip microscopy. *Light: Science & Applications*, 4(3):e261–e261, 2015.
- [3] Alon Greenbaum and Aydogan Ozcan. Maskless imaging of dense samples using pixel super-resolution based multi-height lensfree on-chip microscopy. *Optics express*, 20(3):3129–3143, 2012.
- [4] Zoltán Göröcs and Aydogan Ozcan. On-chip biomedical imaging. *IEEE reviews in biomedical engineering*, 6:29–46, 2012.

- [5] Joseph W Goodman. *Introduction to Fourier optics*. Roberts and Company publishers, 2005.
- [6] Joseph W Goodman. *Statistical optics*. John Wiley & Sons, 2015.
- [7] R Gerhberg and W Saxton. A practical algorithm for the determination of phase from image and diffraction plane picture. *Optik*, 35(2):237–246, 1972.
- [8] Tatiana Latychevskaia. Iterative phase retrieval for digital holography: tutorial. *Journal of the Optical Society of America A*, 36(12):D31–D40, 2019.
- [9] Tatiana Latychevskaia. Criteria for objects suitable for reconstruction from holograms and diffraction patterns. *Journal of the Optical Society of America A*, 41(11):2219–2230, 2024.
- [10] Manuel Guizar-Sicairos and James R Fienup. Understanding the twin-image problem? a3b2 show [pmg: line-break justify=" yes" /]?_c in phase retrieval. *Journal of the Optical Society of America A*, 29(11):2367–2375, 2012.
- [11] Xiwei Huang, Yangbo Li, Xuefeng Xu, Renjie Wang, Jiangfan Yao, Wentao Han, Maoyu Wei, Jin Chen, Weipeng Xuan, and Lingling Sun. High-precision lensless microscope on a chip based on in-line holographic imaging. *Sensors*, 21(3):720, 2021.
- [12] Serhan O Isikman, Waheb Bishara, Sam Mavandadi, Frank W Yu, Steve Feng, Randy Lau, and Aydogan Ozcan. Lens-free optical tomographic microscope with a large imaging volume on a chip. *Proceedings of the National Academy of Sciences*, 108(18):7296–7301, 2011.
- [13] Yair Rivenson, Yichen Wu, Hongda Wang, Yibo Zhang, Alborz Feizi, and Aydogan Ozcan. Sparsity-based multi-height phase recovery in holographic microscopy. *Scientific reports*, 6(1):37862, 2016.
- [14] Waheb Bishara, Ting-Wei Su, Ahmet F Coskun, and Aydogan Ozcan. Lensfree on-chip microscopy over a wide field-of-view using pixel super-resolution. *Optics express*, 18(11):11181–11191, 2010.
- [15] Wenbo Xu, MH Jericho, IA Meinertzhagen, and HJ Kreuzer. Digital in-line holography for biological applications. *Proceedings of the National Academy of Sciences*, 98(20):11301–11305, 2001.
- [16] Jorge Garcia-Sucerquia, Wenbo Xu, Stephan K Jericho, Peter Klages, Manfred H Jericho, and H Jürgen Kreuzer. Digital in-line holographic microscopy. *Applied optics*, 45(5):836–850, 2006.
- [17] Tatiana Latychevskaia and Hans-Werner Fink. Practical algorithms for simulation and reconstruction of digital in-line holograms. *Applied optics*, 54(9):2424–2434, 2015.
- [18] Tatiana Latychevskaia and Hans-Werner Fink. Solution to the twin image problem in holography. *Physical review letters*, 98(23):233901, 2007.
- [19] Gabriel Koren, François Polack, and Denis Joyeux. Iterative algorithms for twin-image elimination in in-line holography using finite-support constraints. *Journal of the Optical Society of America A*, 10(3):423–433, 1993.
- [20] James R Fienup and CC Wackerman. Phase-retrieval stagnation problems and solutions. *Journal of the Optical Society of America A*, 3(11):1897–1907, 1986.
- [21] James R Fienup. Phase retrieval algorithms: a comparison. *Applied optics*, 21(15):2758–2769, 1982.
- [22] James R Fienup. Reconstruction of an object from the modulus of its fourier transform. *Optics letters*, 3(1):27–29, 1978.
- [23] Sanjeev Kumar, Manjunatha Mahadevappa, and Pranab Kumar Dutta. Lensless in-line holographic microscopy with light source of low spatio-temporal coherence. *IEEE Journal of Selected Topics in Quantum Electronics*, 27(4):1–8, 2020.
- [24] Johannes Hagemann and Tim Salditt. Coherence-resolution relationship in holographic and coherent diffractive imaging. *Optics express*, 26(1):242–253, 2018.

- [25] Temitope E Agbana, Hai Gong, Abena S Amoah, Vitaly Bezzubik, Michel Verhaegen, and Gleb Vdovin. Aliasing, coherence, and resolution in a lensless holographic microscope. *Optics letters*, 42(12):2271–2274, 2017.
- [26] Jorge Garcia-Sucerquia. Color digital lensless holographic microscopy: laser versus led illumination. *Applied optics*, 55(24):6649–6655, 2016.
- [27] Jorge Garcia-Sucerquia. Noise reduction in digital lensless holographic microscopy by engineering the light from a light-emitting diode. *Applied Optics*, 52(1):A232–A239, 2013.
- [28] Ibrahim Abdulhalim. Spatial and temporal coherence effects in interference microscopy and full-field optical coherence tomography. *Annalen der Physik*, 524(12):787–804, 2012.
- [29] Jialin Zhang, Jiasong Sun, Qian Chen, and Chao Zuo. Resolution analysis in a lens-free on-chip digital holographic microscope. *IEEE Transactions on Computational Imaging*, 6:697–710, 2020.